M. Wakefield, R. K. Assoian, *Science* 233, 532 (1986).
10. M. B. Sporn *et al.*, *Science* 219, 1329 (1983); W. T. Lawrence *et al.*, *Ann. Surg.* 203, 142 (1986).
11. R. A. Ignotz and J. Massague, *J. Biol. Chem.* 261, 4337 (1986).
12. A. B. Roberts *et al.*, *Proc. Natl. Acad. Sci. U.S.A.* 83, 4167 (1986).
13. R. L. Heimark, D. R. Twardzik, S. M. Schwartz, *Science* 233, 1078 (1986); J. Massagué *et al.*, *Proc. Natl. Acad. Sci. U.S.A.* 83, 8206 (1986); J. H. Kehrl *et al.*, *J. Exp. Med.* 163, 1037 (1986).
14. G. D. Shipley *et al.*, *Cancer Res.* 44, 710 (1984); G. D. Shipley, R. F. Tucker, H. L. Moses, *Proc. Natl. Acad. Sci. U.S.A.* 82, 4147 (1985).
15. R. Ross, *Biol. Rev.* (*Cambridge*) 43, 51 (1968); E. E. Peacock, in *Wound Repair* (Saunders, Philadelphia, ed. 3, 1984), pp. 102–140.
16. We thank J. Reed, J. Lingelbach, and O. Kendrick for excellent technical assistance; J. Smith and L. Dart for preparation of TGF-β from platelets; W. Seyfried, Division of Biostatistics, Washington University Medical School, for statistical assistance; E. Miller and the Jewish Hospital histology laboratory for skillful services; and E. Crouch, Department of Pathology, Jewish Hospital, for helpful discussions.

19 December 1986; accepted 19 June 1987

IRAS Serendipitous Survey Observations of Pluto and Charon

MARK V. SYKES, ROC M. CUTRI, LARRY A. LEBOFSKY, RICHARD P. BINZEL

On 16 August 1983 the Infrared Astronomical Satellite made two separate pointed observations of Pluto and its moon Charon. Because of the small angular displacement of the system between the times of measurement, the Pluto-Charon system was identified as a source in the Serendipitous Survey (SSC 14029+0518). Detections were made at 60 and 100 micrometers with color-corrected flux densities of 581 ± 58 and 721 ± 123 millijanskys, respectively. Pluto is best described as having a dark equatorial band, and brighter polar caps of methane ice extending to ±45° latitude, at most. An upper limit of approximately 9 meter-amagats is placed on the column abundance of a methane atmosphere on Pluto, which is comparable to recent upper limits based on independent ground-based spectroscopy.

THERE HAS BEEN A SURGE OF INTEREST in Pluto in recent years, primarily because of the discovery of its moon Charon (*1*) and the advent of mutual eclipses between the two bodies as Earth passes through the projected orbital plane of Charon (*2*). These eclipse observations will allow for accurate determination of the radii and geometric albedos of Pluto and Charon, as well as the mapping of darker and lighter areas on their surfaces. More interest was generated when a methane atmosphere on Pluto was reported with a column abundance of 27 m-A (*3*), on the basis of ground-based spectroscopy (*4*). Although more recent ground-based observations and analyses have reduced this value by factors of 2 to 4 (*5, 6*), a "significant" atmosphere was reported on the basis of observations made by the Infrared Astronomical Satellite (IRAS) during a survey of the sky at thermal infrared wavelengths (*7*). In this report we analyze more sensitive "pointed" observations made of Pluto by IRAS (*8*), and present quantitative limits on the Pluto atmosphere by means of infrared observations. We conclude that the atmosphere is thinner than originally thought (consistent with the recent ground-based observations) and that surface methane ice is restricted to ice caps whose locations vary in response to large changes in subsolar latitude over a Pluto year (248 Earth years).

M. V. Sykes and R. M. Cutri, Steward Observatory, University of Arizona, Tucson, AZ 85721.
L. A. Lebofsky, Lunar and Planetary Laboratory, University of Arizona, Tucson, AZ 85721.
R. P. Binzel, Planetary Science Institute, Tucson, AZ 85719.

Two separate pointed observations were made of the fields around Pluto on 16 August 1983 at approximately 0430 UT and 1130 UT, in four broad passbands centered on 12, 25, 60, and 100 μm. The images reconstructed from the scans are shown in Fig. 1, and information regarding the Pluto-Charon system at the mean time of observation is given in Table 1. The IRAS Serendipitous Survey examined the point sources extracted from nearly all pointed observation fields that were observed at least twice during the satellite's mission. Infrared sources that were found to lie at nearly the same position and have similar flux densities in two observations of the same field were considered "confirmed" and were compiled in the IRAS Serendipitous Survey Catalog (SSC) (*9*).

A comparison of Pluto's ephemeris position with all of the SSC sources in the Pluto AO fields (Table 2) confirmed the identification of the brightest source (H) seen at 60 and 100 μm as being the Pluto-Charon system (SSC 14029+0518) (*10*). The color-corrected 60- and 100-μm flux densities are 581 ± 58 mJy and 721 ± 123 mJy, respectively (*11*).

Figure 2 shows the Palomar Sky Survey red-plate image in the region of the pointed observation field with the approximate location and uncertainty box of each source indicated. Pluto was not overlying any previously known source that would have contributed to the observed flux at IRAS wavelengths. As can be seen in Fig. 1, Pluto-Charon was detected easily at 60 and 100 μm, and only upper limits are available at 12 and 25 μm (Fig. 3) on account of the large distance between Pluto and the sun. The thermal flux density (B_ν) of a blackbody in radiative equilibrium with sunlight at Pluto's heliocentric distance ($T \sim 51$ K) would peak at around 100 μm and decrease exponentially at shorter wavelengths. Other sources found in the Pluto field (Fig. 2) include two SAO stars (C and D), several faint galaxies (A, B, E, and F), and two sources that are likely associated with modulations in the extended infrared cirrus emission (G and I).

Pluto was also observed while IRAS was in the survey mode (*7*), but a detection was made only at 60 μm. The flux density reported (420 mJy) was much smaller than the value derived from the SSC (Fig. 3). In part, this is probably a result of the lower

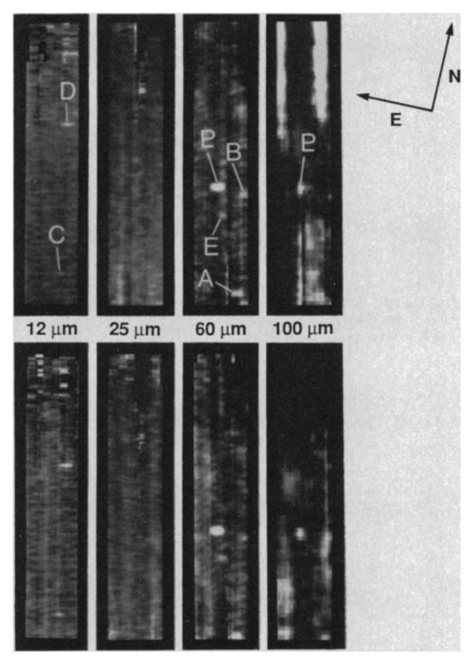

Fig. 1. IRAS observations of the Pluto field taken in the pointed mode on 16 August 1983. Two separate scans (**top** and **bottom**) were taken ~7 hours apart. Several of the SSC sources are clearly seen and marked by their letter designations (Table 2). Pluto-Charon (P) is seen as a strong source at 60 and 100 μm but is invisible at the shorter wavelengths. The only sources seen at 12 μm are SAO stars. At 100 μm, evidence for extended infrared cirrus emission can be seen.

Table 1. Pluto-Charon physical data at the time of the IRAS pointed observations.

Pluto-sun distance	29.87 AU*
Pluto-Earth distance	30.28 AU
Phase angle (*31*)	1.77°
Pluto-Charon apparent separation	0.88 arc sec
Pluto-Charon apparent orientation	Charon due north of Pluto
Pluto radius (*32*)	1145 km
Charon radius (*32*)	642 km
Phase integral (*33*)	0.42
Pluto bolometric Bond albedo (*34*)	0.17
Charon bolometric Bond albedo (*34*)	0.18

*AU: astronomical unit.

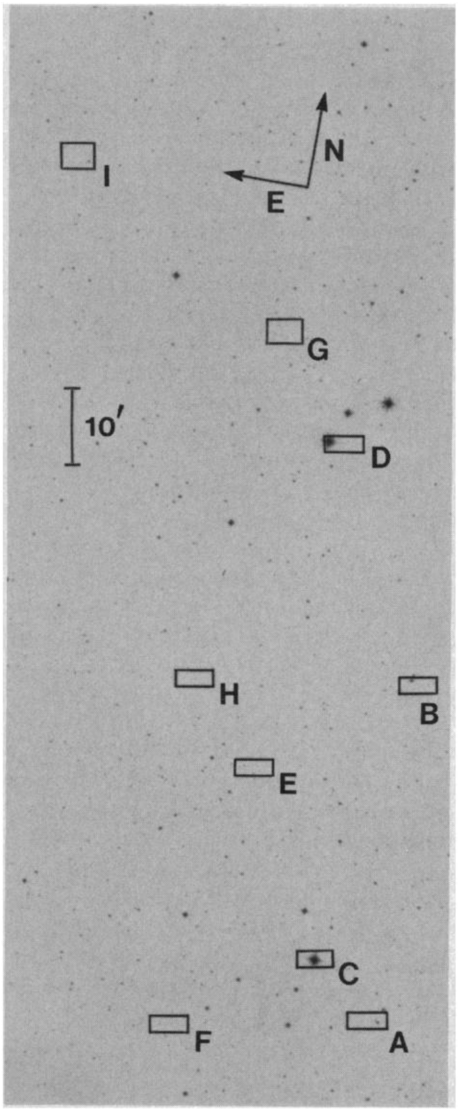

Fig. 2. The region of the Palomar Sky survey red-plate corresponding to the field scanned by IRAS. The more elongated appearance of the field in Fig. 1 is a consequence of the IRAS detectors being rectangular with the long dimension in the cross-scan (east-west) direction. The boxes trace the uncertainty of the source position. These boxes are larger for sources I and G, which were detected only at 100 μm. At the time the plate was taken, Pluto was not in the field. There were no underlying sources at Pluto's location (H) at the time of the IRAS pointed observations.

signal-to-noise ratio survey-mode observations. In addition, the Pluto-Charon system may have been intrinsically brighter in the thermal infrared during the AO scans reported here, since they were taken during the minimum in its visual light curve when a darker surface (hence larger thermal emission) is observed.

The "standard thermal model" assumes that an object can be described by a sphere, and that each point on the surface of that sphere is in instantaneous radiative equilibrium with incident sunlight. All absorbed sunlight is reradiated on the daylit side. This has long been used to describe the thermal emission of asteroids and is a useful tool in determining radiometric diameters of such bodies (*12–15*). For slowly rotating bodies or objects with "dusty" surfaces (similar to the moon), this model works particularly well because of large temperature differences between the day and night sides. However, at large heliocentric distances, equilibrium temperatures are much colder and do not change significantly from day to night. Consequently, the standard thermal model does not apply to objects in the outer solar system, such as Pluto-Charon, because almost as much energy is reradiated from the night side as the day side. In this case thermal emission from an airless body is more accurately described as coming from a sphere whose surface is in radiative equilibrium with the amount of incident sunlight averaged over an entire rotation (*16*). If we assume the observed hemisphere to be uniform in its properties (such as albedo and emissivity), variation in surface temperature becomes solely a function of latitude, Λ. Consequently, this model is referred to as the "isothermal latitude model." The temperature is given by

$$T(\Lambda) = \left(\frac{F_\odot}{R_\odot^2}\,\frac{\alpha}{\pi\sigma} \times \cos\Lambda\right)^{1/4} \qquad (1)$$

where

$$\alpha = \frac{1 - A_b}{\beta\epsilon} \qquad (2)$$

and $F_\odot$ is the solar constant at Earth, $R_\odot$ is the heliocentric distance of Pluto-Charon, σ is the Stefan-Boltzmann constant, A_b is the bolometric Bond albedo, β is the infrared beaming factor (*17*), and ϵ is the emissivity of the surface.

Since Pluto and Charon were not spatially resolved by IRAS, the physical parameters such as albedo and surface area cannot be distinguished between the two bodies on the basis of IRAS observations alone. A mean albedo is assumed for both bodies and the model flux F_n expected to be measured in the *n*th bandpass by IRAS is given by the relation:

$$F_n = \epsilon\,\frac{r_P^2 + r_C^2}{R^2}\int_\lambda\int_{-\pi/2}^{\pi/2}\int_{-\pi/2}^{\pi/2}\tau_n(\lambda)B_\lambda(T) \times \cos\Phi\,\cos^2\Lambda\; d\Phi\, d\Lambda\, d\lambda \qquad (3)$$

where $B_\lambda(T)$ is the Planck function,

$$B_\lambda(T) = \frac{2hc^2}{\lambda^5\left[\exp\left(\frac{hc}{\lambda k T(\Lambda)}\right) - 1\right]} \qquad (4)$$

and r_P is the radius of Pluto, r_C is the radius of Charon, R is the Earth-Pluto distance, $\tau_n(\lambda)$ is the relative response of the *n*th IRAS bandpass as a function of wavelength (*8*), h is Planck's constant, c is the speed of light, k is Boltzmann's constant, and Φ is the longitude (the subsolar point is located at approximately $\Lambda = 0°$, $\Phi = 0°$).

First, we convert the flux densities (in millijanskys) of the IRAS observations to in-band fluxes (in watts per square centimeter) so that the satellite data can be directly compared to the model fluxes (*18*). From the ratio of the IRAS fluxes in the 60- and 100-μm bands and Eqs. 1 and 3 we determine that $\alpha = 1.46^{+0.82}_{-0.57}$. The uncertainty of α is defined by the range of values needed to reproduce the range of uncertainty in the IRAS flux ratio. Using this value of α in Eq. 3, and equating the numerical result to the observed flux in the 60-μm and 100-μm bands, we can constrain the projected surface area of the Pluto-Charon system

Table 2. Serendipitous Survey Catalog sources in the Pluto AOs. Flux densities (in millijanskys) were derived from the AO flux grids 8184 and 8219, which are point source filtered versions of the intensity grids in Fig. 1 (*9*). These values have not been color-corrected. Uncertainties listed are derived from the median noises of the two AO fields.

Object	$F_{12\mu m}$	$F_{25\mu m}$	$F_{60\mu m}$	$F_{100\mu m}$	Name	Notes
A	≤66	≤128	239 ± 12	≤224	14019+0456	Faint galaxy
B	≤66	≤128	138 ± 12	318 ± 35	14019+0520	Faint galaxy
C	124 ± 10	≤128	≤81	≤224	14021+0501	SAO 120271
D	203 ± 10	≤128	≤81	≤224	14024+0536	SAO 120277
E	≤66	≤128	109 ± 12	≤224	14026+0513	Faint galaxy
F	≤66	≤128	78 ± 12	≤224	14028+0455	Faint galaxy
G	≤66	≤128	≤81	308 ± 37	14028+0542	Possible cirrus
H	≤66	≤128	540 ± 11	721 ± 36	14029+0518	Pluto-Charon
I	≤66	≤128	≤81	246 ± 37	14038+0552	Possible cirrus

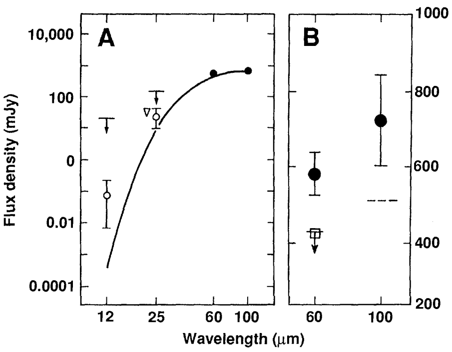

Fig. 3. (**A**) Color-corrected IRAS monochromatic flux densities of Pluto-Charon (●) (and horizontal bars with downward-pointing arrows) are compared with flux densities derived from the isothermal latitude model (○) and a 51 K rapidly rotating blackbody (solid line). At 60 and 100 μm the model and observed flux densities overlap each other. At 12 and 25 μm, the model flux densities are 0.15 and 20 mJy, respectively. A 2σ upper limit (▽) at 22.5 μm of 42 mJy was obtained by Rieke and Rieke (*35*) from the Infrared Telescope Facility (Hawaii) in 1982. Error bars on the model points reflect the propagation of the uncertainty from the IRAS data at 60 and 100 μm. These points are independent of ground-based determinations of the radii and albedos of the system. Model flux densities, with the assumption of Pluto methane ice caps, and ground-base derived parameters listed in Table 1, nearly overlap the values of the isothermal latitude model. Maximum flux densities derived from the Pluto ice cap model are 0.06 mJy (12 μm), 26 mJy (25 μm), 597 mJy (60 μm), and 738 mJy (100 μm). (**B**) The 60- and 100-μm IRAS flux densities (●) are shown on an expanded scale for comparison with the survey coadd flux reported by Tedesco *et al.* (*7*) (□) and the maximum flux density (434 mJy) obtainable from a Pluto model assuming a thick atmosphere (>300 m-A) over a pure methane ice surface. Charon is described by the isothermal latitude model with parameters shown in Fig. 4. The dashed line is the corresponding 100-μm flux density (512 mJy) for the thick atmosphere model. In this latter case, model parameters can be adjusted to improve the predicted 100-μm flux, but only at the expense of the 60-μm flux.

(weighted by its mean surface emissivity) to be $\epsilon A_{PC} = 4.3^{+1.1}_{-1.6} \times 10^6$ km^2. With the total surface area of the system derived from Table 1, this value for the projected area yields emissivity values of $\epsilon = 0.79^{+0.21}_{-0.29}$. By comparison, most surfaces have emissivities between 0.9 and 1.0 (*19*). The low values we obtain for the emissivity might arise from the presence of methane ice on Pluto (*20*), which is thought to have a low emissivity (*21*). The distribution of this methane ice will be discussed later. From Eq. 1, the nominal subsolar temperature of both Pluto and Charon is 59 K. A nominal beaming factor of $\beta = 0.72$, which is derived from Eq. 2 and the values for α and ϵ, is comparable to the value of 0.75 derived for asteroids but smaller than the value of 0.86 derived for the icy satellites of Jupiter and Saturn (*15*). These latter values are based on observations made of asteroids and icy satellites at 10 and 20 μm. The beaming factor should get closer to unity (indicating a weaker effect) at longer wavelengths for a cratered topography (*22*). A stronger beaming effect for Pluto-Charon at 60 and 100 μm would indicate unusual surface topography, perhaps deep grooves over most of the surface.

The model of Trafton and Stearn for Pluto, in which a methane atmosphere which exceeds 7 cm-A over a thick methane ice surface, results in a globally isothermal surface (*21*). The thermal flux expected from such an object is given by

$$F_n = \epsilon \frac{\pi r_P^2}{R^2} \int_\lambda \tau_n(\lambda) B_\lambda(T) d\lambda \qquad (5)$$

where

$$T = \left(\frac{F_\odot \, \alpha}{R_\odot^2 4\sigma} \right)^{1/4} \qquad (6)$$

One consequence of an isothermal surface is the removal of the effect of infrared beaming (there being no temperature differences between shadowed and sunlit surfaces). Thus, in Eq. 2, $\beta = 1$. Diameters and albedos for Pluto and Charon were taken from Table 1. Charon's beaming factor was allowed to vary from 0.72 to 1.0. Since water ice is likely to be a significant component of Charon's surface and methane ice is depleted (*23*), we assume an emissivity of 0.9 for Charon.

For each combination of Charon thermal properties, the emissivity of Pluto was varied from 0.1 to 1.0 in order to attempt to reproduce the in-band fluxes observed by IRAS and thereby constrain the surface temperatures and atmospheric column abundance. In each case the predicted fluxes fell short of the IRAS 60-μm flux by greater than 2.5 standard deviations regardless of the resultant thickness of Pluto's atmosphere (Fig. 3). We thus conclude that the Pluto atmosphere is not thick enough to isothermalize the planet's surface. If the atmospheric column abundance falls below 7 cm-A, the temperature distribution converges onto that of the isothermal latitude model. However, for a pure methane ice surface, this also requires subsolar temperatures lower than 48 K, since the methane column abundance is a sensitive function of temperature. This conflicts with the result of the previous isothermal latitude model, which requires a nominal equatorial temperature 11 K warmer, in order to reproduce the IRAS pointed observations.

The last model we discuss assumes that all of the methane on Pluto is located in polar caps, leaving an equatorial band depleted in methane. This allows us to invoke the warmer temperature required by the previous IRAS-constrained isothermal latitude model while also maintaining an areal coverage of methane, which is known to be present on the surface (*20*). The caps are assumed to be isothermal (*24*) and symmetric about both poles. Each cap spans the same amount of latitude, and is expected to have a higher albedo and lower emissivity than the equatorial region. This region is described by the isothermal latitude model as is Charon. Its thermal properties (β, ϵ) are assumed to be the same as Charon's, since Charon is also methane-depleted (*23*) and the composition of the two bodies should be similar if they formed at the same location of the solar nebula. That is, we expect water ice to be a significant component of the equatorial surface (*25*). We also require that the area-weighted average albedo of Pluto be equal to the value in Table 1. An additional imposed condition is that temperatures be continuous across methane ice cap boundaries.

As the caps extend to lower latitudes, their temperature increases, and the column density of a possible methane atmosphere also increases. We assume that Pluto's equatorial band and Charon have the same emissivity of 0.9 (from arguments given above) and a beaming factor that is allowed to vary

Fig. 4. The Pluto methane ice cap model with model results and parameters needed to minimize the latitude of the cap boundary and maximize the atmospheric column abundance, ρ. A_b is the bolometric Bond albedo, β is the infrared beaming factor, ϵ is the emissivity, T_{ss} is the subsolar temperature, and T_{cap} is the temperature over the ice caps. The relative radii of Pluto and Charon are to scale, but their separation at the time of the Serendipitous Survey observations is not.

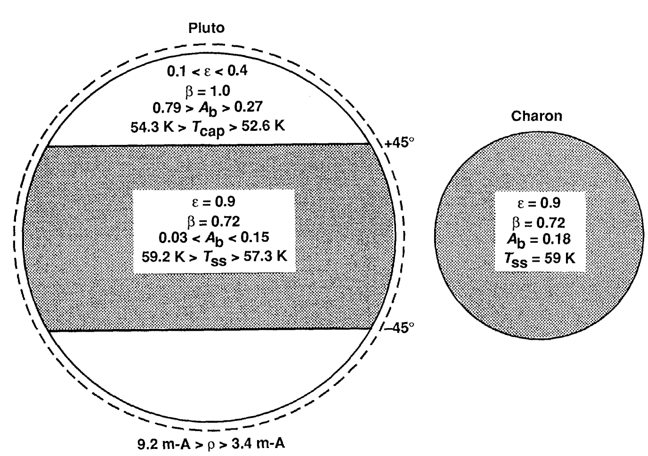

from 0.72 to 1.0. Methane ice cap emissivities are varied from 0.1 to 1.0. Once the cap emissivity is fixed along with noncap and Charon emissivity and beaming, and the lower latitude of the caps, the bolometric Bond albedos of the caps and equatorial band are determined. Combinations of the above variables are rejected if albedos calculated are negative or greater than unity, or if the caps are darker than the equatorial band.

When the beaming factor is near its lower value and cap emissivities have values between 0.1 and 0.4, the IRAS fluxes are reproduced to within 3%, whereas the lowest allowable latitude for the caps is found to be ±45°. The calculated albedos and temperatures for the methane ice caps and equatorial band, given the above range of parameters, are shown in Fig. 4. A maximum atmospheric column density of 9.2 m-A is determined, if we assume the emissivity of methane ice to be 0.1. Higher emissivities, latitudes, and beaming factors result in a lower column abundance (*26*). We have also considered the effect of Pluto's variation in albedo with rotational phase and find no significant change in the ice cap model results (*27*). The 9.2 m-A upper limit determined here is somewhat lower than the estimate of 15 ± 5 m-A by Cochran and Sawyer (*6*) and is greater than Buie and Fink's upper limit of 5.5 m-A (*5*).

The existence of ice caps on Pluto with a darker equatorial band is qualitatively consistent with the "spot" models of Marcialis (*28*) and Buie (*29*). Both models, although not unique solutions, have dark equatorial spots, the largest of which was nearly centered on Pluto's disk at the time of the IRAS observations reported here. Both posited bright polar caps as one means of explaining the secular dimming of the system. The present methane ice caps, by our model, exist as a consequence of the greater insolation at the equator, and a thin enough layer of methane ice that it sublimates at equatorial temperatures on time scales very short compared to a Pluto year. Because of the large obliquity of the system (86°), the poles actually receive more insolation than the equator, averaged over a Pluto year. Thus, we expect the distribution of methane ice on Pluto's surface to change significantly as the subsolar latitude varies during the Pluto year. When the subsolar latitude is ±86°, all methane ice should be located on the "dark" pole, hidden from terrestrial view. Consequently, future "spot" models may have to consider the case of nonstatic ice caps whose coverage varies with time; it would be of great benefit to the interpretation of Pluto-Charon observations if laboratory spectroscopy of methane ice is undertaken at visual and far-infrared wavelengths (*30*).

REFERENCES AND NOTES

1. J. Christy and R. Harrington, *Astron. J.* **83**, 1005 (1978).
2. R. P. Binzel, D. J. Tholen, E. F. Tedesco, B. J. Buratti, R. M. Nelson, *Science* **228**, 1193 (1985).
3. One meter-amagat (m-A) equals 2.687×10^{21} molecules per square centimeter; 1 cm-A equals 2.687×10^{19} molecules per square centimeter.
4. U. Fink *et al.*, *Icarus* **44**, 62 (1980).
5. M. Buie and U. Fink, *ibid.* **70**, 483 (1987).
6. W. Cochran and S. Sawyer, *Bull. Am. Astron. Soc.* **18**, 822 (1986).
7. E. Tedesco, G. Veeder, R. Dunbar, L. Lebofsky, *Nature (London)* **327**, 127 (1987).
8. The Infrared Astronomical Satellite (IRAS) was launched into a nearly polar orbit in January 1983 to survey the sky at many wavelengths in the thermal infrared that are not accessible from ground-based telescopes. In addition to its normal survey mode, IRAS made nearly 10,000 pointed observations of objects of scientific interest. These observations were called additional observations (AO). These observations were made by scanning across an object, often several times, at ~1/2 the normal survey scan rate of 3.85 arc min/sec, allowing objects to be measured at lower brightness levels and higher signal-to-noise ratios. A detailed description of the IRAS satellite, its mission, and data products may be found in C. Beichmann, G. Neugebauer, H. Habing, P. Clegg, T. Chester, Eds., *The Infrared Astronomical Satellite Explanatory Supplement* (Jet Propulsion Laboratory, Pasadena, CA, 1984).
9. S. G. Kleinmann, R. M. Cutri, E. T. Young, F. J. Low, F. C. Gillett, *Explanatory Supplement to the IRAS Serendipitous Survey Catalog* (Jet Propulsion Laboratory, Pasadena, CA, 1986).
10. During the time interval separating the two independent pointed observations of Pluto-Charon, the apparent motion of the system (24 arc sec) was smaller than the positional search box defined for SSC source "confirmation." At 60 μm this box measured 70 arc sec in the in-scan direction and 142.5 arc sec in the cross-scan direction. Therefore, the Pluto-Charon system was identified as a "stationary" point source in the SSC processing. The resulting flux densities and position of the source listed in the SSC (Table 2) are an average of the flux densities and positions extracted from the independent observations, weighted by the inverse square of the median noise levels of the respective AO fields (grids) in each band.
11. The uncertainties arise from several factors that influence how the reported measurements relate to the true emission levels of the sources, such as noise in the detector system and in the sky background, and possible systematic effects related to the method of measurement used by the satellite. The SSC provides several independent evaluations of these uncertainties. The uncertainty level quoted in Table 2 is the median noise from the catalog, which is derived from the noise levels sensed by the satellite's detectors averaged over the entire AO field. This value provides a good measure of the strength of the source signal relative to the ambient detector and background noise levels. A better estimate of total measurement uncertainty for SSC sources is the ratio of the flux densities measured for each source in the two independent observations of each AO field. The values for Pluto-Charon are 0.9 and 0.8 at 60 and 100 μm, respectively. If a large number of independent measurements of a source could be made, the dispersion in those measurements would reflect the effects of both statistical errors and other systematic uncertainties. Although this is not possible for any single source, the same results were obtained in the SSC Explanatory Supplement (*9*) by analyzing the flux ratios of a large number of sources. The characteristic uncertainties associated with 60- and 100-μm sources of the brightness of the Pluto-Charon system determined in this fashion are ~10 and ~17%, respectively. An independent source of error in the quoted flux densities arises from uncertainty in the internal consistency of the absolute calibration of the SSC. Comparison with independently reduced measurements of standard stars indicates this uncertainty amounts to less than 1% at 60 μm and ~2% at 100 μm (*9*), values that make a negligible contribution to total measurement uncertainties.
12. All models in this report are calculated for 0° phase angle. A phase coefficient of 0.01 magnitude per degree is characteristic of asteroids at thermal wavelengths [D. Tholen, *International Astronomical Circular No. 4302* (Harvard Smithsonian Center for Astrophysics, Cambridge, MA, 1987)]. If this same coefficient is adopted for the IRAS observations of Pluto-Charon, it would lead to a change of <2% in the flux, and consequently the effect is neglected.
13. D. Morrison and L. Lebofsky, in *Asteroids*, T. Gehrels, Ed. (Univ. of Arizona Press, Tucson, 1979), p. 184.
14. R. H. Brown, D. Morrison, C. Telesco, W. Brunk, *Icarus* **52**, 188 (1982).
15. L. Lebofsky *et al.*, *ibid.* **68**, 239 (1986).
16. M. Sykes and L. Lebofsky, in preparation.
17. Surface topography results in an enhancement of thermal flux (beaming) near zero phase over that expected from a smooth surface. Likewise, at higher phase angles, more cool shadowed surfaces are seen, resulting in lower thermal fluxes observed than expected.
18. The factors to convert from monochromatic flux density in janskys in each pass band to watts per square centimeter are 1.348×10^{-14} (12 μm to band 1), 5.155×10^{-14} (25 μm to band 2), 2.577×10^{-14} (60 μm to band 3), and 1.00×10^{-14} (100 μm to band 4).
19. A. Kahle, *J. Geophys. Res.* **82**, 1673 (1977).
20. D. P. Cruikshank, C. B. Pilcher, D. Morrison, *Science* **194**, 835 (1976).
21. L. Trafton and S. Stearn, *Astrophys. J.* **267**, 872 (1983).
22. O. Hansen, *Icarus* **31**, 456 (1977).
23. R. L. Marcialis, G. H. Rieke, L. A. Lebofsky, *Science* **237**, 1349 (1987).
24. L. Trafton, *Icarus* **58**, 312 (1984).
25. Water ice is the principal condensate from the solar nebula at Pluto's heliocentric distance, with other ices (CH_4, NH_3, and CO, for example) present in minor amounts assuming solar abundances [J. Lewis and R. Prinn, *Astrophys. J.* **238**, 357 (1980)].
26. For a latitude of ±50 and a cap emissivity of 0.2 and a beaming factor of 0.76, the column abundance is 3.6 m-A. Higher infrared beaming factors also result in lower column abundances (greater than a factor of 2 for $\Delta\beta = 0.1$).
27. At 0.75 rotation phase, Pluto is near maximum light and has an average bolometric Bond albedo of 0.23. Requiring the area-weighted average albedo of Pluto in the ice cap model to equal this value results in a decrease of only 5° in the lowest possible latitude of the methane ice caps, and an increase of ~4 m-A in the maximum atmospheric column density. Since this model is unconstrained by any thermal observations at this rotation phase, however, these numbers merely indicate the stability of our model results for 0.0 rotational phase.
28. R. Marcialis, thesis, Vanderbilt University, Nashville (1983).
29. M. W. Buie, thesis, University of Arizona, Tucson (1984).
30. Interpretation of visual spectroscopic observations have been hampered by the lack of laboratory spectra of methane ice at these wavelengths. Researchers instead have been using spectra of gaseous and liquid methane in order to determine the relative contributions of gaseous and solid methane to the absorption spectra observed (*5, 6*).
31. The phase angle of observation is the apparent angular separation of Earth and sun as seen at Pluto.
32. D. J. Tholen, M. W. Buie, R. P. Binzel, M. L. Frueh, *Science* **237**, 512 (1987).
33. The phase integral is estimated by averaging the known phase integrals of the first 50 asteroids in the *IRAS Asteroid and Comet Survey*, D. Matson, Ed. (Jet Propulsion Laboratory, Pasadena, CA, 1986).
34. The bolometric Bond albedo is the ratio of total reflected light to the total incident light on a sphere, integrated over all wavelengths. We assume the bolometric Bond albedos of Pluto and Charon are equal to the product of the blue geometric albedos given in (*32*) and the phase integral (*33*). Pluto displays rotational brightness variations of ~30%, and at the time of the AOs, it was at minimum light (rotation phase 0.0). Tholen *et al.* (*32*) give the

average blue geometric albedos of Pluto and Charon at superior conjunction (rotation phase 0.75, near maximum light). Pluto's bolometric Bond albedo was corrected for the observed light curve amplitude between phases 0.75 and 0.0, Charon's albedo was assumed to remain constant. Definitions for Pluto's rotational phases and light curve amplitude were taken from R. Binzel and J. Mulholland [*Astron. J.* **89**, 1759 (1984)].
35. G. Rieke and M. Rieke, private communication.
36. We thank F. Low, D. Hunten, E. Young, D. Tholen, M. Buie, B. Marcialis, J. Lunine, and J. Spencer for useful discussions. D. Davis, S. Weidenschilling, D. Spaute, W. Hartman and W. Cochran are thanked for their review of the manuscript. We thank G. Kopan for provided timing information for the AOs. T. Green helped with image processing. We are grateful to K. Denomy and T. Schemenaur for preparing the figures. M.V.S. and R.M.C. were supported by Jet Propulsion Laboratory contract 954601. L.A.L. was supported by NASA grant NSG7114. This is Planetary Science Institute contribution 240. PSI is a division of Science Applications International Corporation.

1 May 1987; accepted 27 July 1987

A Transgenic Mouse Model for Human Neurofibromatosis

STEVEN H. HINRICHS, MICHAEL NERENBERG, R. KAY REYNOLDS, GEORGE KHOURY, GILBERT JAY*

Human T-lymphotropic virus type 1 (HTLV-1) has been associated with the neurologic disorder tropical spastic paraparesis and possibly with multiple sclerosis. The *tat* gene of HTLV-1 under control of its own long terminal repeat is capable of inducing tumors in transgenic mice. The morphologic and biologic properties of these tumors indicate their close resemblance to human neurofibromatosis (von Recklinghausen's disease), the most common single gene disorder to affect the nervous system. The high spontaneous incidence of this disease, together with the diverse clinical and pathologic features associated with it, suggests that environmental factors may account for some of the observed cases. Multiple tumors developed simultaneously in the transgenic *tat* mice at approximately 3 months of age, and the phenotype was successfully passed through three generations. The tumors arise from the nerve sheaths of peripheral nerves and are composed of perineural cells and fibroblasts. Tumor cells from these mice adapt easily to propagation in culture and continue to express the tat protein in significant amounts. When transplanted into nude mice, these cultured cells efficiently induce tumors. Evidence of HTLV-1 infection in patients with neural and other soft tissue tumors is needed in order to establish a link between infection by this human retrovirus and von Recklinghausen's disease and other nonlymphoid tumors.

While human T-lymphotropic virus type 1 (HTLV-1) has been associated with the development of lymphoma and leukemia in humans, less than 0.1 percent of individuals who have antibodies to the virus develop lymphoid malignancies and do so only after a long latency period (*1*). The clinical and morphologic features of the disease are varied and may involve the skin and bone as well as the lymphoid system (*2*). Recent studies have suggested that HTLV-1–induced disease may be accompanied by neurologic symptoms (*3–5*).

A previously obscure syndrome termed tropical spastic paraparesis (TSP) affects the nervous system and has been epidemiologically linked to infection with HTLV-1 through detection of antibodies in serum and cerebral spinal fluid (*3*). The characteristic symptoms in patients with TSP from the Caribbean appear to be related to the central nervous system with gradual development of spastic paralysis as well as facial nerve paralysis and selective sensory deficits (*3*). A similar disorder termed HTLV-1–associated myelopathy (HAM) has been described in patients from Japan (*4*). Serologic and low stringency hybridization data have provided evidence of HTLV-1–related antigens and sequences in patients with multiple sclerosis (MS) (*5*). Thus clinical evidence would suggest that HTLV-1 may be neurotropic as well as lymphotropic.

The *tat* gene of HTLV-1 under the control of its own long terminal repeat (LTR) is capable of inducing two phenotypes in transgenic mice in the absence of other viral genes (*6*). Tumors arose in all three founder mice (designated 6-2, 6-7, and 8-4) which survived longer than 3 months, an observation that is consistent with tumor development being unrelated to the site of integration of the transgene. On the basis of their spindle cell morphology, the tumors were thought to be of mesenchymal derivation. Most of the tumors were benign, although in some cases malignant features were seen.

We analyzed the offspring from two of the original three founder mice (6-2 and 8-4), as well as those from the more recently derived 12-2 founder. The tumor phenotype was faithfully transmitted to 30 of 30 F_1 transgenic progeny mice and was successfully carried into the F_2 and F_3 generations. Tumors first appeared between 90 and 130 days of age. They were usually located on the ears, nose, legs, or tail (Fig. 1A). Most tumors began as small discrete nodules, which became confluent or multinodular as they enlarged. The largest tumor that we have observed was on the tail, and it measured approximately 1 cm in its greatest dimension; it had a high mitotic index and extended to the surrounding connective tissue, features we interpreted as consistent with a malignant transformation. Granulocytic infiltration occurred in all large and small tumors, despite little or no evidence of tumor necrosis.

Primary tumors expressed concentrations of the tat protein that were several times higher than any normal tissue, as revealed by Western blot analysis. Isolated tumor cells placed in tissue culture expressed tat in the nucleus, as demonstrated by indirect immunofluorescence (Fig. 2). Tissue culture cells that produced the tat protein have been passaged at least ten times and have grown tumors in five of five nude mice.

Three of four females from the F_1 and F_2 generations of the 6-2 lines were noticeably different from their male counterparts. They expressed the *tat* gene as shown by immunoblot analysis of tail extracts, but did not show external signs of tumor development. Nevertheless, they succumbed to progressive wasting and death by 3 months of age. At autopsy, all three animals showed tumors of the cranial nerves (two animals) or nerve ganglion (one animal). In one of these animals, the intracranial tumor had its origin in the left fifth cranial nerve ganglion (Fig. 1B). In that particular case, the right fifth cranial nerve showed no evidence of tumor. Histologically, the tumor was composed of elongated, spindle-shaped cells admixed with ganglion cells. No evidence of extension into the brain was seen. A second tumor was found in the cranial foramen, but its site of origin could not be determined. The remaining two females had diffuse involvement of a plexiform type of the extracranial nerves V and VII. Coronal sections from one of these mice demonstrated extensive tumor involvement of the nerve as it passed to the right of oral cavity and tongue, while the nerves on the left side appeared normal (Fig. 1C).

Since the tumors from these three animals suggested a close association with nerve, we

Laboratory of Molecular Virology, National Cancer Institute, Bethesda, MD 20892.

*To whom correspondence should be addressed.